

Optimizing detection limits in whispering gallery mode biosensing

Matthew R. Foreman,^{1*} Wei-Liang Jin² and Frank Vollmer¹

¹Max Planck Institute for the Science of Light, Laboratory of Nanophotonics and Biosensing, Günther-Scharowsky-Straße 1, 91058 Erlangen, Germany

²State Key Laboratory for Mesoscopic Physics and School of Physics, Peking University, Beijing 100871, Peoples Republic of China

*Corresponding author: matthew.foreman@mpl.mpg.de

Abstract: A theoretical analysis of detection limits in swept-frequency whispering gallery mode biosensing modalities is presented based on application of the Cramér-Rao lower bound. Measurement acuity factors are derived assuming the presence of uncoloured and $1/f$ Gaussian technical noise. Frequency fluctuations, for example arising from laser jitter or thermorefractive noise, are also considered. Determination of acuity factors for arbitrary coloured noise by means of the asymptotic Fisher information matrix is highlighted. Quantification and comparison of detection sensitivity for both resonance shift and broadening sensing modalities are subsequently given. Optimal cavity and coupling geometries are furthermore identified, whereby it is found that slightly under-coupled cavities outperform critically and over coupled ones.

© 2014 Optical Society of America

OCIS codes: (000.5490) Probability theory, stochastic processes, and statistics; (110.3055) Information theoretical analysis; (240.3990) Micro-optical devices; (260.5740) Resonance; (280.1415) Biological sensing and sensors.

References and links

1. M. Baaske and F. Vollmer "Optical Resonator Biosensors: Molecular Diagnostic and Nanoparticle Detection on an Integrated Platform," *ChemPhysChem* **13**, 427–436 (2012).
2. K. J. Vahala "Optical microcavities" *Nature* **424**, 839–846 (2003).
3. F. Vollmer, S. Arnold, and D. Keng "Single virus detection from the reactive shift of a whispering-gallery mode," *Proc. Natl. Acad. Sci. USA* **105**, 20701–20704 (2008).
4. M. Noto, F. Vollmer, D. Keng, I. Teraoka, and S. Arnold "Nanolayer characterization through wavelength multiplexing of a microsphere resonator," *Opt. Lett.* **30**, 510–512 (2005).
5. F. Vollmer, S. Arnold, D. Braun, I. Teraoka, and A. Libchaber "Multiplexed DNA quantification by spectroscopic shift of two microsphere cavities," *Biophys. J.* **85**, 1974–1979 (2003).
6. F. Vollmer, D. Braun, A. Libchaber, M. Khoshima, I. Teraoka, and S. Arnold "Protein detection by optical shift of a resonant microcavity," *Appl. Phys. Lett.* **80**, 4057–4059 (2002).
7. S. Arnold, M. Khoshima, I. Teraoka, S. Holler, and F. Vollmer. "Shift of whispering-gallery modes in microspheres by protein adsorption," *Opt. Lett.* **28**, 272–274, (2003).
8. W. Ahn, S. V. Boriskina, Y. Hong, and B. M. Reinhard "Photonic-plasmonic mode coupling in on-chip integrated optoplasmonic molecules," *ACS Nano*. **6**, 951–960 (2012).
9. F. Vollmer and L. Yang "Label-free detection with high-Q microcavities: a review of biosensing mechanisms for integrated devices," *Nanophot.* **1**, 267–291 (2012).
10. M. L. Gorodetsky, A. A. Savchenkov, and V. S. Ilchenko "Ultimate Q of optical microsphere resonators," *Opt. Lett.* **21**, 453–455 (1996).
11. M. R. Foreman and F. Vollmer "Theory of resonance shifts of whispering gallery mode sensors by arbitrary plasmonic nanoparticles," *New. J. Phys.* **15**, 083006 (2013).
12. M. A. Santiago-Cordoba, S. V. Boriskina, F. Vollmer, and M. C. Demirel "Nanoparticle-based protein detection by optical shift of a resonant microcavity," *Appl. Phys. Lett.* **99**, 073701 (2011).

13. V. R. Dantham, S. Holler, C. Barbre, D. Keng, V. Kolchenko, and S. Arnold "Label-free detection of single protein using a nanoplasmonic-photonic hybrid microcavity," *Nano. Lett.* **13**, 3347–3351 (2013).
14. J. Zhu, S. J. Ozdemir, Y.-F. Xiao, L. Li, L. He, D.-R. Chen, and L. Yang "On-chip single nanoparticle detection and sizing by mode splitting in an ultrahigh- Q microresonator," *Nat. Phot.* **4**, 46–49 (2010).
15. J. Knittel, J. D. Swaim, D. L. McAuslan, G. A. Brawley, and W. P. Bowen "Back-scatter based whispering gallery mode sensing," *Sci. Rep.* **3**, 2974 (2013).
16. L. Xu, H. Li, X. Wu, L. Shang, and L. Liu "Ultra-sensitive label-free biosensing by using single-mode coupled microcavity laser," *Proc. SPIE*, **7682**, 76820C (2010).
17. T. McGarvey, A. Conjusteau, and H. Mabuchi "Finesse and sensitivity gain in cavity-enhanced absorption spectroscopy of biomolecules in solution," *Opt. Express*, **14**, 10441–10451 (2006).
18. J. D. Swaim, J. Knittel, and W. P. Bowen "Detection limits in whispering gallery biosensors with plasmonic enhancement," *Appl. Phys. Lett.* **99**, 243109 (2011).
19. L. Shao, X.-F. Jiang, X.-C. Yu, B.-B. Li, W. R. Clements, F. Vollmer, W. Wang, Y.-F. Xiao, and Q. Gong "Detection of single nanoparticles and lentiviruses using microcavity resonance broadening," *Adv. Mat.* **25**, 5616–5620 (2013).
20. S. Arnold, R. Ramjit, D. Keng, V. Kolchenko, and I. Teraoka "Microparticle photophysics illuminates viral biosensing," *Faraday Disc.* **137**, 65–83, (2008).
21. J. L. Nadeau, V. S. Ilchenko, D. Kossakovski, G. H. Bearman, and L. Maleki "High- Q whispering-gallery mode sensor in liquids," *Proc. SPIE* **4629**, 172 (2002).
22. N. M. Hanumegowda, C. J. Stica, B. C. Patel, I. White, and X. Fan "Refractometric sensors based on microsphere resonators," *Appl. Phys. Lett.* **87**, 201107 (2005).
23. X. Lopez-Yglesias, J. M. Gamba, and R. C. Flagan "The physics of extreme sensitivity in whispering gallery mode optical biosensors," *J. Appl. Phys.* **111**, 084701 (2012).
24. A. B. Matsko, A. A. Savchenkov, N. Yu, and L. Maleki "Whispering gallery mode resonators as frequency references. I. Fundamental limitations," *J. Opt. Soc. Am. B* **24**, 1324–1335 (2007).
25. M. L. Gorodetsky and I. S. Grudinin "Fundamental thermal fluctuations in microspheres," *J. Opt. Soc. Am. B* **21**, 697–705 (2004).
26. W.-L. Jin, X. Yi, Y. Hu, B. Li, and Y. Xiao, "Temperature-insensitive detection of low-concentration nanoparticles using a functionalized high- Q microcavity," *Appl. Opt.* **52**, 155–161 (2013).
27. A. A. Savchenkov, A. B. Matsko, V. S. Ilchenko, N. Yu, and L. Maleki "Whispering-gallery-mode resonators as frequency references. II. Stabilization," *J. Opt. Soc. Am. B*, **24**, 2099–2997 (2007).
28. T. Carmon, L. Yang, and K. J. Vahala "Dynamical thermal behavior and thermal self-stability of microcavities," *Opt. Express* **12**, 4742–4750 (2004).
29. I. Teraoka "Analysis of thermal stabilization of whispering gallery mode resonance," *Opt. Commun.* **310** 212–216 (2014).
30. L. L. Scharf, *Statistical Signal Processing: Detection, Estimation, and Time Series Analysis*, (Addison-Wesley Publishing Co., USA, 1991).
31. C. Vignat and J.-F. Bercher "Analysis of signals in the Fisher-Shannon information plane," *Phys. Lett. A* **312**, 27–33 (2003).
32. H. Cramér, *Mathematical Methods of Statistics*, (Princeton University Press, USA, 1946).
33. M. R. Foreman and P. Török, "Information and resolution in electromagnetic optical systems," *Phys. Rev. A* **82**, 043835 (2010).
34. M. Abramowitz and I. Stegun, *Handbook of Mathematical Functions*, (Dover Publications, New York, 1970).
35. T. Lu, H. Lee, T. Chen, S. Herchak, J.-H. Kim, S. E. Fraser, R. C. Flagan, and K. Vahala "High sensitivity nanoparticle detection using optical microcavities," *Proc. Natl. Acad. Sci. USA* **108**, 5976–5979 (2011).
36. A. Zeira and A. Nehorai, "Frequency domain Cramer-Rao bound for Gaussian Processes," *IEEE Trans. Acoust. Speech. Sig. Proc.* **38** 1063–1066 (1990).
37. Y.-F. Xiao "Optical cavity QED in Solid-State Systems - Theory to Realization," PhD thesis (University of Science and Technology of China, 2007).
38. M. L. Gorodetsky and V. S. Ilchenko "Optical microsphere resonators: optimal coupling to high- Q whispering-gallery modes," *J. Opt. Soc. Am. B* **16**, 147–154 (1999).
39. M. Bass, C. M. DeCusatis, and J. M. Enoch *Handbook of Optics*, 3rd ed., Vol. 4. (McGraw-Hill, USA 2009).
40. G. M. Hale and M. R. Querry "Optical Constants of Water in the 200-nm to 200- μ m Wavelength Region," *Appl. Opt.* **12**, 555–563 (1973).
41. M. Cai, O. Painter, and K. J. Vahala "Observation of Critical Coupling in a Fiber Taper to a Silica-Microsphere Whispering-Gallery Mode System," *Phys. Rev. Lett.* **85**, 74–77 (2000).
42. J. Topolancik and F. Vollmer "Photoinduced transformations in bacteriorhodopsin membrane monitored with optical microcavities," *Biophys. J.* **92**, 2223–2229 (2007).
43. D. Q. Chowdhury, S. C. Hill, and P.W. Barber, "Morphology-dependent resonances in radially inhomogeneous spheres," *J. Opt. Soc. Am. A* **8**, 1702–1705 (1991).
44. I. Teraoka and S. Arnold "Theory of resonance shifts in TE and TM whispering gallery modes by nonradial perturbations for sensing applications," *J. Opt. Soc. Am. B* **23**, 1381–1389 (2006).

45. S. Arnold, S. I. Shopova, and S. Holler “Whispering gallery mode bio-sensor for label-free detection of single molecules: thermo-optic vs. reactive mechanism,” *Opt. Express* **18**, 281–287 (2010).
46. A. Mazzei A, S. Göttinger, L. de S. Menezes, G. Zumofen, O. Benson, and V. Sandoghdar “Controlled Coupling of Counterpropagating Whispering-Gallery Modes by a Single Rayleigh Scatterer: A Classical Problem in a Quantum Optical Light,” *Phys. Rev. Lett.* **99**, 173603 (2007).
47. X. Yi, Y.-F. Xiao, Y. Feng, D.-Y. Qiu, J.-Y. Fan, Y. Li, and Q. Gong “Mode-splitting-based optical label-free biosensing with a biorecognition-covered microcavity,” *J. Appl. Phys.* **111**, 114702 (2012).
48. U. Resch-Genger, M. Grabolle, S. Cavaliere-Jaricot, R. Nitschke, and T. Nann “Quantum dots versus organic dyes as fluorescent labels,” *Nat. Methods* **5**, 763–775 (2008).
49. M. R. Foreman and F. Vollmer “Level repulsion in hybrid photonic-plasmonic microresonators for enhanced biodetection,” *Phys. Rev. A* **88**, 023831 (2013).
50. D. S. Weiss, V. Sandoghdar, J. Hare, V. Lefèvre-Seguin, J. M. Raimond, and S. Haroche “Splitting of high-Q Mie modes induced by light backscattering in silica microspheres,” *Opt. Lett.* **20**, 1835–1837 (1995).
51. Y.-F. Xiao, Y.-C. Liu, B.-B. Li, Y.-L. Chen, Y. Li, and Q. Gong “Strongly enhanced light-matter interaction in a hybrid photonic-plasmonic resonator,” *Phys. Rev. A* **85**, 031805 (2012).
52. A. N. Bashkatov and E. A. Genina “Water refractive index in dependence on temperature and wavelength: a simple approximation,” *Proc. SPIE* **5068**, 393–395 (2003).
53. C. Lam, P. T. Leung, and K. Young “Explicit asymptotic formulas for the positions, widths, and strengths of resonances in mie scattering,” *J. Opt. Soc. Am. B*, **9**, 1585–1592 (1992).

1. Introduction

Recent years have seen great advances in the development of micro and nanoscale biosensors, motivated by the promise of single molecule sensitivity. Sensitive and label-free detection of individual biomolecules such as viruses, DNA and proteins, is particularly important for implementing next-generation (potentially on-chip) clinical diagnostic assays. Of particular importance are optical resonator based biosensors, which are rapidly emerging as one of the most sensitive biosensing technologies, capable of providing not-only label-free detection down to the single molecule level [1–3], but also allowing multiplexed sensing [4, 5], aqueous working environments [6, 7] and cost-effective integration on micro-chips [8, 9]. Whispering gallery mode (WGM) resonators, for example, exhibit high sensitivity by virtue of their high quality (Q) resonances (fundamentally limited to $\sim 10^{10}$ [10]) and large surface intensities, which can be further augmented by plasmonic nanoantennae [11–13]. As with all experimental methods, however, noise fundamentally limits the achievable sensitivity levels. Knowledge of such noise imposed detection limits allows for improved system design and benchmarking and thus warrants closer study.

WGM based sensors can employ a number of different operational principles, for example, frequency locking or swept-frequency modalities, transmission vs. back-scattering detection, passive or active cavities and also ring-down measurements. Perhaps the more commonly used and easiest to implement of these strategies is the swept-frequency modality, in which the transmission of a source coupled to a resonator is monitored as the frequency of the source is varied. Whilst detection limits have been extensively studied for a number of these configurations [14–17], analysis of swept-frequency based biosensors is inherently more complex and has thus not yet been comprehensively covered. To date, attempts to quantify the detection limits of swept-frequency WGM sensors have predominantly been based on either qualitative arguments or empirical estimates [18–22] and hence lack the satisfaction associated with more rigorous treatments. A number of papers have attempted to adopt a more theoretical approach with Lopez-Yglesias et. al. [23], for example, considering different physical interactions between a WGM sensor and an adsorbed molecule which can affect induced sensing signals. Noise sources were, however, given only minimal consideration. Various fundamental noise sources, such as thermorefractive noise, were considered in the works of Matsko et. al. [24] and Gorodetsky et. al. [25], however these treatments are not immediately transferable to a biosensing context thus hampering their utility. This paper thus attempts to bridge this gap and

formulate biodetection limits when using swept-frequency WGM microsensors based upon a rigorous consideration of the noise sources deriving from information theoretic tools. Attention is limited to two dominant noise sources, namely additive Gaussian detector noise and thermorefractive noise/laser fluctuations, since these are frequently the limiting factors within biosensing experiments. Noise is assumed to be uncoloured, however calculation for arbitrary power spectra is discussed and illustrated for pink ($1/f$) noise. Moreover, to the authors knowledge, all preceding treatments, perhaps with the exception of [19], have considered detection limits based upon monitoring reactive resonance shifts only. Measurements of linewidth change are however currently emerging as a complementary sensing mechanism. We therefore also formulate detection limits in this regard. Beyond the insight into system performance that quantification of detection limits affords, such knowledge allows for optimisation of sensor geometry and other operational parameters. Optimisation of this nature therefore constitutes a further aim of this work.

The structure of this article is as follows. In Section 2 we first formulate the measurement problem and describe the origin and nature of relevant noise sources, before proceeding to describe fundamental detection limits imposed on measuring reactive shifts and linewidth changes by means of an information theoretic analysis in Section 3. Detection limits derived in Section 3, although sufficient to describe the problem, are rather formal in nature, therefore in Section 4 we apply our results to biosensing experiments. Consequently, optimal WGM sensing configurations are identified for different sensing scenarios, and the performance of reactive shift and line broadening sensing modalities compared. Section 5 continues by considering robustness of optimal configurations to environmental temperature changes, before Section 6 finally considers how optimisation results are altered in the presence of additional loss mechanisms, such as surface roughness or nanoantenna induced heating and scattering losses. Final conclusions are drawn in Section 7. A number of appendices are also given providing further elaboration on our mathematical derivations where necessary.

2. Measurement and noise in WGM sensing

Whispering gallery mode biosensors commonly operate by monitoring the transmission properties of a swept laser source coupled to a microresonator e.g. via a tapered fibre or prism based setup [1]. When the laser frequency ω is tuned close to a resonance of the microcavity (with frequency ω_0 and full width at half maximum (FWHM) Γ), a Lorentzian dip is observed in the transmission profile of the input beam (see Fig. 1) as described by

$$I(\omega) = I_0 \left[1 - \frac{A\Gamma^2/4}{(\omega - \omega_0)^2 + \Gamma^2/4} \right], \quad (1)$$

where I_0 is the incident beam power and A describes the coupling efficiency to the microcavity (or transmission depth). An important point to note, however, is that whilst Eq. (1) describes a continuous lineshape, in practice discrete samples are taken at a fixed interval $\Delta\Omega \triangleq \beta\Gamma$ over a finite bandwidth $\Omega \triangleq W\Gamma$. In what follows we shall denote the discrete sampling frequencies and associated power level as ω_j and $I_j = I(\omega_j)$ respectively. For a single laser sweep a total of N_Ω data points, $I_{d,j}$, are collected ($j = 1, 2, \dots, N_\Omega$), which for convenience we stack into a data vector $\mathbf{I}_d = (I_{d,1}, I_{d,2}, \dots, I_{d,N_\Omega})$. For each laser scan the parameters ω_0 , Γ and A can then be estimated, for example, by numerical fitting. Determination of resonance shifts and broadening from, say, the presence of a biomolecule [6, 7, 19] follows by comparing the determined parameters for subsequent scans. The accuracy to which each of the parameters can be determined, however, is limited by noise which is inescapably present in the measurement process. Such noise can be of either a technical or fundamental nature and consideration should be given to both in determining detection limits of WGM sensors.

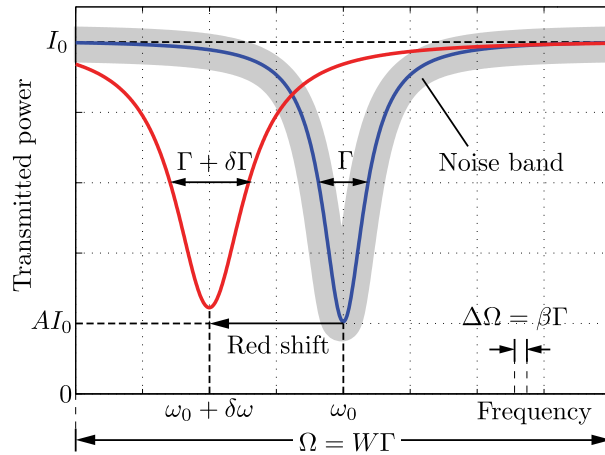


Fig. 1. Schematic of observed transmission lineshape, induced red shift and line broadening upon binding of biomolecules to the microcavity surface, illustrating definitions of quantities used in this work.

Technical noise arises from poor experimental setup and can include factors such as stray light impinging upon photodetectors and vibrations. Generally, such noise sources are statistically independent and are well described by a Gaussian probability distribution function (PDF) by virtue of the Central Limit Theorem. Noting that typical power levels in WGM biosensing experiments are $\lesssim 1$ mW, it is furthermore reasonable to adopt a classical description of light, such that the net effect of technical noise on the measured power $I_{d,j}$ can be described by the continuous PDF

$$p_{I_d}(I_{d,j}; \omega_0, \Gamma, A) = \frac{1}{\sqrt{2\pi\sigma_d^2}} \exp\left[-\frac{1}{2}\left(\frac{I_{d,j} - I_j}{\sigma_d}\right)^2\right], \quad (2)$$

where σ_d^2 is the variance of the detected intensity. If multiple independent noise sources contribute to the total technical noise, σ_d^2 is found by adding the associated variances of individual noise sources. Detector noise is perhaps the most intuitive and common noise such that we shall hereafter refer to technical noise simply as detector noise.

Fundamental noise limitations, on the other hand, can arise from a number of different physical phenomena. Thermodynamic fluctuations within the cavity and surrounding medium, for example, give rise to both thermorefractive and thermoelastic noise, from variations in the refractive index and cavity size respectively [25, 26]. Additionally, temperature fluctuations can cause changes in the coupling distance, albeit these can be negated by means of free space coupling [19]. Microresonators are furthermore interrogated by means of laser light which, due to its quantised nature, can result in photothermal, optoelastic and phase noise. A good discussion of the effects of these noise sources can be found in [24], however, for our purposes it is sufficient to consider only thermorefractive noise since this was found to be dominant (although methods of suppressing its influence have been proposed [27]). Fluctuations in the refractive index within the mode volume have a dual effect of modifying both the frequency and linewidth of the microcavity resonance. Frequently in the literature, fluctuations in the resonance linewidth are assumed to be negligible; an assumption based on empirical observation [28, 29]. Theoretical justification of this approximation is, however, given in Appendix A,

such that we too only consider fluctuations in the resonance frequency. Making the replacement $\omega_0 \rightarrow \omega_0 + \omega_t$ in Eq. (1), where ω_t represents the thermorefractive resonance shift from the unperturbed resonance frequency, allows us to describe the effect of thermorefractive noise via the PDF

$$p_{\omega_t}(\omega_t) = \frac{1}{\sqrt{2\pi\sigma_t^2}} \exp\left[-\frac{1}{2} \frac{\omega_t^2}{\sigma_t^2}\right], \quad (3)$$

where a Gaussian PDF is again assumed. Equivalently, the resultant random fluctuations in the measured power are described by

$$\begin{aligned} p_{I_d}(I_{d,j}; \omega_0, \Gamma, A) &= \int_{-\infty}^{\infty} \delta(I_{d,j} - I_j) p_{\omega_t}(\omega_t) d\omega_t \\ &= \frac{1}{\sqrt{2\pi\sigma_t^2}} \frac{I_0 A \Gamma_j^2}{4\Lambda_j (I_0 - I_{d,j})^2} \exp\left[-\frac{1}{2} \frac{\Delta_j^2}{\sigma_t^2}\right] \exp\left[-\frac{1}{2} \frac{\Lambda_j^2}{\sigma_t^2}\right] \cosh\left[\frac{\Lambda_j \Delta_j}{\sigma_t^2}\right], \end{aligned} \quad (4)$$

where Eq. (4) derives from the law of total probability, $\Delta_j = \omega_j - \omega_0$ and $\Lambda_j = \frac{\Gamma}{2} [I_0 A / (I_0 - I_{d,j}) - 1]^{1/2}$. Whilst we have considered fluctuations in the central resonance frequency of the WGM arising from thermorefractive noise, it is worthwhile noting that frequency fluctuations can also arise from other sources, such as instabilities in the laser (typically ~ 100 kHz – 1 MHz for tunable laser sources). Results given for thermorefractive noise are hence equally applicable to laser fluctuations (jitter). In the presence of both thermorefractive noise and laser jitter, σ_t^2 is again found by adding the associated variances of each noise source. Whilst not explicitly discussed here, our results have shown that symmetric sweeping of the resonance peak (i.e. the laser frequency sweeps the interval $\omega \in [\omega_0 - \Omega/2, \omega_0 + \Omega/2]$) achieves greatest measurement accuracy. Only this case is therefore considered in what follows.

3. Fisher information and detection limits

Fisher information is a natural metric emerging from the field of statistical estimation, which quantifies the performance of an ideal observer in estimating an original signal given a noise corrupted version [30]. Although Fisher information shares many properties with the better known Shannon information, such as superadditivity and positivity [31], the former is more suitable for describing the measurement problem (as opposed to the information transmission problem). In particular, the covariance matrix, $\mathbb{K}_{\mathbf{w}}$, for estimation of a parameter vector \mathbf{w} , which provides a convenient parameterisation of measurement precision, is lower bounded by the inverse of the Fisher information matrix $\mathbb{J}_{\mathbf{w}}$ viz.

$$\mathbb{K}_{\mathbf{w}} \geq \mathbb{J}_{\mathbf{w}}^{-1}, \quad (6)$$

where the inequality implies the difference of the two matrices is positive definite and does not necessarily hold element-wise. In our case $\mathbf{w} = (\omega_0, \Gamma, A)$. Eq. (6) is known as the Cramér-Rao lower bound (CRLB) [32] and also implies the weaker set of inequalities $\sigma_{w_i}^2 \geq 1/[\mathbb{J}_{\mathbf{w}}]_{ii}$ where $\sigma_{w_i}^2$ is the variance for estimation of w_i and w_i ($[\mathbb{J}_{\mathbf{w}}]_{ii}$) denotes the i th (diagonal) element of \mathbf{w} ($\mathbb{J}_{\mathbf{w}}$). It is important to note that the CRLB as expressed by Eq. (6) explicitly quantifies the uncertainty achievable by *any* unbiased estimator and hence represents a fundamental limit to measurement precision. Furthermore, by use of the maximum likelihood estimator the CRLB can be asymptotically achieved [30]. A fuller discussion of Fisher information and properties of the maximum likelihood estimator can be found in [30, 33] and references therein.

Within the context of biosensing, we do not directly measure the parameters $\mathbf{w} = (\omega_0, \Gamma, A)$, but instead infer them from noisy power readings. As such the Fisher information matrix can

be written in the form $\mathbb{J}_{\mathbf{w}} = \mathbb{G}^T \mathbb{J}_{\mathbf{I}} \mathbb{G}$, where $\mathbb{G} = \partial \mathbf{I} / \partial \mathbf{w}$ is a matrix of derivatives, T denotes the matrix transpose and $\mathbb{J}_{\mathbf{I}}$ is the Fisher information matrix associated with estimation of the transmitted power \mathbf{I} . Initially, we assume that the noise on each data point is statistically independent such that we can write $p_{\mathbf{I}_d}(\mathbf{I}_d) = \prod_{j=1}^{N_\Omega} p_{I_d}(I_{d,j}; \omega_0, \Gamma, A)$, yielding

$$[\mathbb{J}_{\mathbf{I}}]_{ij} = \delta_{i,j} \int p_{I_d,j}(I_{d,j}) \left(\frac{\partial \ln p_{I_d,j}(I_{d,j}; \omega_0, \Gamma, A)}{\partial I_j} \right)^2 dI_{d,j}, \quad (7)$$

where $\delta_{i,j}$ is the Kronecker delta. The case of dependent data samples will be discussed below. Since each data sample is statistically independent we can invoke additivity of Fisher information to give $\mathbb{J}_{\mathbf{w}} = \sum_{j=1}^{N_\Omega} J_{I_j} \mathbf{G}_j \otimes \mathbf{G}_j$ where \otimes denotes the outer product and the shorthand notation $[\mathbb{J}_{\mathbf{I}}]_{jj} = J_{I_j}$ and $\mathbf{G}_j = \partial I_j / \partial \mathbf{w}$ has been used.

In principle, the PDFs given by Eqs. (2) and (5) can be substituted directly into Eq. (7) and calculated numerically, however, to gain further insight into the noise limitations we make a number of approximations, such that analytic results follow. First considering the simpler case of detector noise, as described by Eq. (2), we assume that the laser sweeping window has a large bandwidth relative to the FWHM of the WGM resonance i.e. $\Omega > 2\Gamma$, and that the sampling interval is small i.e. $\Delta\Omega \ll \Gamma$. Under these conditions the summation in Eq. (7) can be approximated by a continuous integral over frequency. Taking evaluation of $[\mathbb{J}_{\mathbf{w}}]_{11} = J_{\omega_0, \omega_0}$ as an illustrative example we find

$$J_{\omega_0, \omega_0} = \sum_{j=1}^{N_\Omega} \frac{1}{\sigma_d^2} \left(\frac{\partial I_j}{\partial \omega_0} \right)^2 \approx \frac{A^2 I_0^2}{4\sigma_d^2 \Delta\Omega} \Gamma^4 \int_{-\infty}^{\infty} \frac{(\omega_0 - \omega)^2}{[(\omega_0 - \omega)^2 + \Gamma^2/4]^4} d\omega = \frac{A^2 I_0^2}{2\sigma_d^2 \Delta\Omega} \frac{\pi}{\Gamma}. \quad (8)$$

Similarly, evaluation of other elements of the Fisher information matrix can be performed, ultimately yielding

$$\mathbb{J}_{\mathbf{w}} = \frac{\pi I_0^2}{8\sigma_d^2 \Delta\Omega} \begin{pmatrix} 4A^2/\Gamma & 0 & 0 \\ 0 & A^2/\Gamma & A \\ 0 & A & 2\Gamma \end{pmatrix}. \quad (9)$$

Off diagonal elements of the Fisher information matrix represent correlations that exist between estimates of different parameters, such that here we see that estimates of the transmission depth and FWHM are correlated. Such a correlation is to be expected, since determination of the FWHM requires an estimate of the dip depth. In practical biosensing, the transmission depth is, however, of marginal or no interest and can hence be treated as a nuisance parameter [30]. Nuisance parameters, by virtue of the correlations mentioned above, reduce the amount of information any measurement yields about the parameters of interest, and thus reduce the detection limits. Within the framework of statistical estimation theory it can be shown that a reduced Fisher information matrix can be defined, which in our case, and for the sake of completeness, takes the form

$$\mathbb{J}_{\mathbf{w}'} = \begin{pmatrix} J_{\omega_0, \omega_0} - \frac{J_{\omega_0, A}^2}{J_{A, A}} & J_{\omega_0, \Gamma} - \frac{J_{\Gamma, A} J_{\omega_0, A}}{J_{A, A}} \\ J_{\omega_0, \Gamma} - \frac{J_{\Gamma, A} J_{\omega_0, A}}{J_{A, A}} & J_{\Gamma, \Gamma} - \frac{J_{\Gamma, A}^2}{J_{A, A}} \end{pmatrix} = \frac{A^2 I_0^2}{16\sigma_d^2 \Delta\Omega} \frac{\pi}{\Gamma} \begin{pmatrix} 8 & 0 \\ 0 & 1 \end{pmatrix}. \quad (10)$$

In the remainder of this work, we will, however, not consider calculation of the reduced Fisher information matrix, since it adds a level of mathematical complexity, which provides little additional insight. Instead, attention will be given to calculation of $[\mathbb{J}_{\mathbf{w}}]_{11} = J_{\omega_0, \omega_0}$ and $[\mathbb{J}_{\mathbf{w}}]_{22} = J_{\Gamma, \Gamma}$. Applying the inequality $\sigma_{w_i}^2 \geq 1/[\mathbb{J}_{\mathbf{w}}]_{ii}$ thus yields an expression for the minimum detectable

resonance shift, $\Delta\omega_d$, and linewidth change, $\Delta\Gamma_d$,

$$\Delta\omega_d = \frac{\Delta\Gamma_d}{2} = \sqrt{\frac{2\beta}{\pi}} \frac{\sigma_d}{I_0 A} \Gamma. \quad (11)$$

We can approach the problem for derivation of the detection limits in the presence of thermorefractive noise/laser jitter in a similar manner, however additional approximations and care must be taken. We start by considering

$$J_{\omega_0, \omega_0} = \sum_{j=1}^{N_\Omega} \int_0^\infty \left[\frac{1}{\sigma_t^2} - \frac{\Lambda_j^2}{\sigma_t^4} \operatorname{sech}^2 \left(\frac{\Lambda_j \Delta_j}{\sigma_t^2} \right) \right] p_{I_{d,j}} dI_{d,j}. \quad (12)$$

The summation for the first term can be easily performed, since by definition $\int p_{I_{d,j}} dI_{d,j} = 1$, however, to evaluate the second term we again approximate the summation over j as an integration over frequency, yielding

$$J_{\omega_0, \omega_0} \approx \frac{N_\Omega}{\sigma_t^2} - \frac{1}{\Delta\Omega \sigma_t^5} \sqrt{\frac{2}{\pi}} \int_0^\infty \Lambda^2 \exp \left(-\frac{\Lambda^2}{2\sigma_t^2} \right) \int_{-\infty}^\infty \operatorname{sech} \left(\frac{\Lambda\Delta}{\sigma_t^2} \right) \exp \left(-\frac{\Delta^2}{2\sigma_t^2} \right) d\Delta d\Lambda, \quad (13)$$

where a change in the integration variable has also been performed. Further approximating $\operatorname{sech} x \approx \exp[-x^2/2]$, where the FWHM of the Gaussian has been chosen such that the Taylor expansion of the functions match up to quadratic order, allows evaluation of Eq. (13) such that

$$J_{\omega_0, \omega_0} \approx \frac{1}{\sigma_t} \left[\frac{N_\Omega}{\sigma_t} - \frac{\sqrt{\pi}}{\Delta\Omega} U \left(\frac{1}{2}, 0, \frac{1}{2} \right) \right] = \frac{1}{\sigma_t \Delta\Omega} \left[\frac{\Omega}{\sigma_t} - 1.416 \right], \quad (14)$$

where $U(a, b, z)$ is the confluent hypergeometric function [34]. Finite integration limits for integration over Δ can also be taken, leading to an additional term in the kernel of the integration over Λ of the form $\operatorname{erf} \left[\frac{\Omega}{2\sqrt{2}\sigma_t} \sqrt{1 + \frac{\Lambda^2}{\sigma_t^2}} \right]$. Noting, however, that the argument of the error function is large, we can approximate this term as unity, hence also yielding Eq. (14). We note that due to the approximations taken the Fisher information expressed by Eq. (14) can adopt negative (i.e. unphysical) values when $\Omega \leq 1.416\sigma_t$. Fortunately, this condition is only satisfied in pathological noise scenarios, such that Eq. (14) gives a good estimate of the Fisher information for estimation of ω_0 (in the presence of thermorefractive noise/laser jitter) in most cases. Our detection limit is then given by

$$\Delta\omega_t = \sqrt{\frac{\beta\Gamma\sigma_t}{W\Gamma/\sigma_t - 1.416}} \approx \sigma_t \sqrt{\frac{\beta}{W}}, \quad (15)$$

where the second approximation holds for $\sigma_t \ll W\Gamma$. Eq. (15) shows that the detection limit scales with the number of sampling points as $N_\Omega^{-1/2} = (\beta/W)^{1/2}$.

Derivation of $J_{\Gamma, \Gamma}$ follows in a similar manner to that shown here for J_{ω_0, ω_0} , however greater care must be taken with the size of the integration window, so as to avoid divergent integrals. For completeness the derivation is presented in Appendix B and only the final result is given here; chiefly

$$J_{\Gamma, \Gamma} \approx \frac{2\sigma_t}{3\Gamma^2 \Delta\Omega} \frac{\Omega}{2\sigma_t} \left[3 + \left(\frac{\Omega}{2\sigma_t} \right)^2 \right], \quad (16)$$

such that

$$\Delta\Gamma_t = 2\sigma_t \sqrt{\frac{3\beta}{W} \frac{\Gamma^2}{24\sigma_t^2 + W^2\Gamma^2}} \approx 2\sigma_t \sqrt{\frac{3\beta}{W^3}}, \quad (17)$$

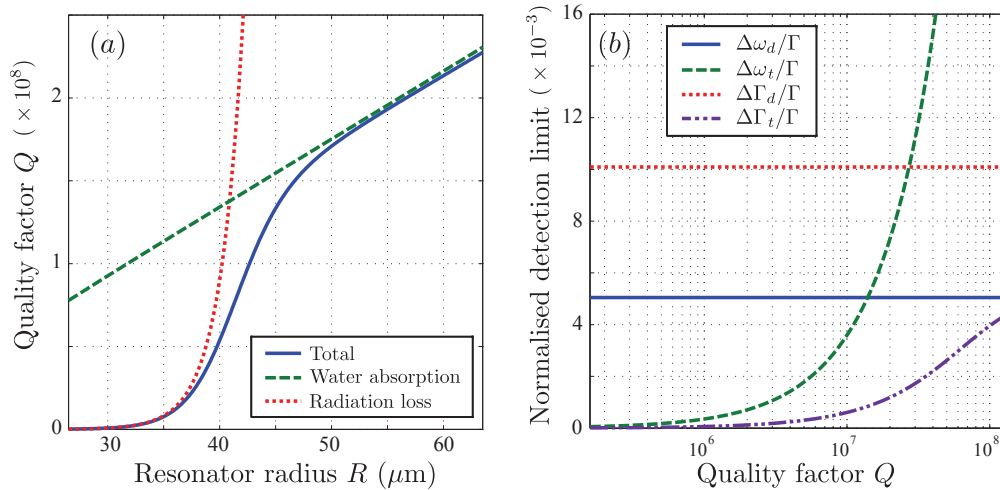


Fig. 2. (a) Variation of intrinsic quality factor Q_0 of a fused silica WGM resonance in water with microcavity radius R . (b) Variation of detection limits $\Delta\omega_{d,t}$ and $\Delta\Gamma_{d,t}$ (normalised to resonance linewidth) with WGM Q factor.

where the second approximation again holds when $\sigma_t \ll W\Gamma$. By virtue of the dependence of $\Delta\omega_{t,d}$ and $\Delta\Gamma_{t,d}$ on the resonance linewidth, the detection limits imposed by noise inherit a dependence on the size of the microresonator, as depicted in Fig. 2. Specifically Fig. 2(a) shows the dependence of the intrinsic (i.e. limited by radiation and absorption losses) quality factor $Q_0 = \omega_0/\Gamma$ for a fused silica microsphere resonator of radius R immersed in water, supporting a fundamental TE WGM (first radial order) resonance at 780 nm. Curves in Fig. 2 were found by numerically solving the exact Mie resonance conditions of a microsphere [11]. Note, that the resonance spectrum of a microsphere contains discrete spectral peaks since only particular wavelengths can satisfy the associated resonance conditions. Similarly only microcavities with the correct size can support a WGM at a fixed wavelength, such that the curves in Fig. 2 are not continuous but composed of discrete points. These points are densely packed however, producing the appearance of a continuous curve. For cavities smaller than $\sim 40 \mu\text{m}$ it can be seen that radiation losses dictate the resonance lifetime, whilst for larger resonators water absorption becomes dominant, producing an approximate linear relationship between intrinsic quality factor and resonator size. This linear dependence arises since for larger l WGMs a greater proportion of the mode volume lies within the cavity and not in the surrounding absorbing host. It should be noted that for very large resonators of radius $\gtrsim 1$ mm, absorption within the cavity volume dominates, however for common biosensing applications resonators of this size are not desirable and hence we neglect cavity absorption in what follows. Figure 2(b), meanwhile, plots the size dependence of the various detection limits $\Delta\omega_{t,d}$ and $\Delta\Gamma_{t,d}$ (normalised to linewidth). Simulation parameters were $\beta = 10^{-3}$, $W = 20$, $\sigma_d = I_0/5$. To model the thermorefractive noise/laser jitter an equivalent temperature fluctuation of $\Delta T = 5$ mK was taken such that $\sigma_t = (\omega_0 \Delta T / n_c) dn_c / dT$, where $\tilde{n}_c = n_c + i\kappa_c$ is the complex refractive index of the microcavity and $dn_c / dT = 1.45 \times 10^{-5}$ [25]. This value of ΔT gives comparable noise levels to detector noise. Specifically, for these simulation parameters we find $\Delta\omega_d \approx 2.5$ fm, $\Delta\Gamma_d \approx 5$ fm, $\Delta\omega_t \approx 2$ fm and $\Delta\Gamma_t \approx 0.3$ fm for $Q = 10^7$ at 780 nm. Clear differences between detector and thermorefractive noise can be seen in Fig. 2. In particular, the detection limits for detector noise scale linearly with linewidth (normalised detection limits are hence a constant function of Q),

whilst those for thermorefractive noise exhibit a more complicated dependence, albeit monotonically increasing, i.e. smaller spheres are less susceptible to thermorefractive noise due to a small modal volume (a point further discussed later). We note, however, that suppression of laser jitter can be achieved experimentally [35], such that pure thermodynamical fluctuations dominate. In this case a value of $\Delta T \sim 30 \mu\text{K}$ is more appropriate [25].

The above analysis was based on the simplifying assumption that each data sample was statistically independent or equivalent all noise sources are white in nature. In reality, noise sources in WGM sensors can be colored, for example, electronic components can give rise to pink ($1/f$) noise, whilst thermorefractive noise inherently has a non-uniform power spectrum [25]. Consequently, the covariance matrix $\mathbb{K}_{\mathbf{I}}$ (and hence $\mathbb{J}_{\mathbf{I}}$) is no longer diagonal. Knowledge of the spectral power density of the noise sources, e.g. [15, 25], however, allows easy implementation of a whitening filter [30] so as to decorrelate data samples, such that all previous (and subsequent) results are applicable. Use of whitening filters of this nature are commonplace in signal processing.

Determination of exact detection limits in the presence of colored noise is, nevertheless, still possible within the framework of the Fisher information and the CRLB. To illustrate the methodology we briefly consider the case of pink detector noise, as may arise from electronic based detection, and assume the underlying random process is at least wide-sense stationary. Furthermore, we again invoke the fine sampling limit used above, whereby we can use the asymptotic form of the FIM [36]

$$[\mathbb{J}_{\mathbf{I}}]_{jk} \approx \frac{1}{2\pi} \int_{-\pi}^{\pi} \frac{1}{\Phi(s)} \exp[is(j-k)] ds, \quad (18)$$

where $\Phi(s) = \sum_{r=-\infty}^{\infty} [\mathbb{K}_{\mathbf{I}}]_{j,j+r} \exp[-isr]$ is the power spectral density of the noise process. $\Phi(s)$ can be easily related to the continuous power spectral density (see e.g. Eq. 14(b) of [36]). Owing to the assumption of wide-sense stationarity, $\mathbb{K}_{\mathbf{I}}$ is Toeplitz, such that $\Phi(s)$ is independent of j . Letting $\Phi(s) = A/|s|$ for $s_1 \leq s \leq s_2$, that is say assume pink noise, we find

$$[\mathbb{J}_{\mathbf{I}}]_{jk} \approx \frac{\pi}{Ap^2} (\cos p + p \sin p - 1), \quad (19)$$

where $p = (j-k)\pi$. From the Wiener-Khinchin theorem it can further be shown that $\mathbb{K}_{jj} = A \ln(s_2/s_1)$, which we also equate to σ_d^2 . The laser sweep time τ is always finite in practice, such that the lower frequency region of the noise spectrum can not be observed and it is reasonable to adopt $s_1 = 2\pi/\tau$. The upper frequency bound can furthermore be selected to match Nyquist's frequency in turn yielding $s_2/s_1 = 2\Omega/\Delta\Omega = 2W/\beta$. Numerical computation of $\mathbb{J}_{\mathbf{w}} = \mathbb{G}^T \mathbb{J}_{\mathbf{I}} \mathbb{G}$ can then be easily performed for a given set of experimental parameters. For the parameters considered above, we find that $\Delta\omega_d \approx 0.0113\Gamma$ and $\Delta\Gamma_d \approx 0.0391\Gamma$, which importantly reproduces the linear dependence on linewidth seen in Eq. (11). Analogous results to those derived below for white noise thus hold for pink noise when an appropriate noise variance is used.

4. Optimal whispering gallery mode biosensors

4.1. Resonance shifts

Treatment of the detection problem, as given in the preceding sections, is largely theoretical such that a formulation with greater ease of application to biosensing problems is desirable. With this aim in mind, we recall the formalism presented in [20], wherein the minimum detectable number of bioparticles, N , is defined as the ratio of the minimum resolvable frequency shift to the shift induced by a single biomolecule. The latter is given by the well known reactive

sensing principle [7];

$$\frac{\delta\omega}{\omega_0} = -\varepsilon_0\varepsilon_s \text{Re}[\alpha] \frac{|E(\mathbf{r}_p)|^2}{4U}, \quad (20)$$

where ε_0 is the permittivity of free space, $\tilde{\varepsilon}_s = \varepsilon_s + i\eta_s$ is the relative permittivity of the host medium, $|E(\mathbf{r}_p)|^2$ is the local field intensity at the position of the bioparticle of excess polarizability α and $U = \frac{1}{2}\varepsilon_0\varepsilon_s \int |\mathbf{E}(\mathbf{r})|^2 dV$ is the total electromagnetic energy density stored in the WGM. For small ($\ll \lambda$) spherical particles of radius b we have $\alpha = 4\pi b^3(\tilde{\varepsilon}_{pt} - \tilde{\varepsilon}_s)/(\tilde{\varepsilon}_{pt} + 2\tilde{\varepsilon}_s)$, where $\tilde{\varepsilon}_{pt}$ is the permittivity of the particle. Eq. (20) can be shown to be consistent with a quantum treatment [14]. In [20] it was thus shown for a particle binding on the equator of a microsphere of radius R supporting a WGM of order l and quality factor $Q = \omega_0/\Gamma$ and immersed in a host medium of refractive index $\tilde{n}_s = n_s + i\kappa_s$ that the minimum number of detectable bioparticles is given by

$$N = \frac{\Delta\omega}{|\delta\omega|} = \frac{(n_c^2 - n_s^2)}{\text{Re}[\alpha]} \frac{R^3}{|Y_{ll}(\pi/2)|^2} \frac{F}{Q}, \quad (21)$$

where $Y_{ll}(\theta)$ represents the usual spherical harmonic functions, albeit with the dependence of the azimuthal angle ϕ omitted, since this is irrelevant to the modulus. High Q WGMs are associated with high orders such that we can make the approximation

$$|Y_{ll}(\theta)|^2 \approx \frac{1}{4\pi^{3/2}} \frac{2l+1}{l^{1/2}} \sin^{2l} \theta \quad (22)$$

for computational ease. Furthermore, $F = |\Delta\omega|/\Gamma$ represents a so-called measurement acuity factor. Whilst in [20] empirical values of F were taken, we can, by means of Eqs. (11) and (15), now provide a theoretical expression, which can either be used for comparison with experimental observations or for system design. For example, in the presence of detector noise we have $F = F_0/A$ where $F_0 = \sqrt{2\beta/\pi} \sigma_d/I_0$ is the measurement acuity for a critically coupled microresonator. Within an experimental context, it should be observed that if the sampling interval is scaled with the linewidth of the resonance, that is to say β is fixed (recall $\Delta\Omega \triangleq \beta\Gamma$), F_0 is a constant determined by the experimental configuration, as is consistent with the assumptions made in [20]. Importantly, however, if the sampling interval $\Delta\Omega$ is a fixed experimental parameter, then the measurement acuity scales as $\Gamma^{-1/2}$, i.e. it is dependent on the quality of the sensing WGM. In what follows we shall consider only the former case. Another important feature arising from our treatment is that the dependence of the measurement acuity on coupling losses comes to the fore. In particular we have $Q^{-1} = Q_0^{-1} + Q_c^{-1}$ and $A = 4Q_0Q_c/(Q_0 + Q_c)^2$ [37], where Q_0 is the intrinsic quality factor of the WGM and Q_c describes coupling losses. For example, for a prism coupled WGM it has been shown that Q_c can be related to the coupling distance, d , viz. [38]

$$Q_c = \sqrt{\frac{2\pi^5 n_c}{n_p^2 - n_c^2}} (n_c^2 - n_s^2) \left(\frac{R}{\lambda}\right)^{3/2} \exp[2\gamma d], \quad (23)$$

where n_p is the refractive index of the coupling prism and $\gamma = (2\pi/\lambda)\sqrt{n_c^2 - n_s^2}$. For additive Gaussian (detector) noise we thus finally find

$$N = \frac{(n_c^2 - n_s^2)}{\text{Re}[\alpha]} \frac{R^3}{|Y_{ll}(\pi/2)|^2} \frac{F_0}{Q_0} \frac{(1 + Q_c/Q_0)^3}{4Q_c^2/Q_0^2}. \quad (24)$$

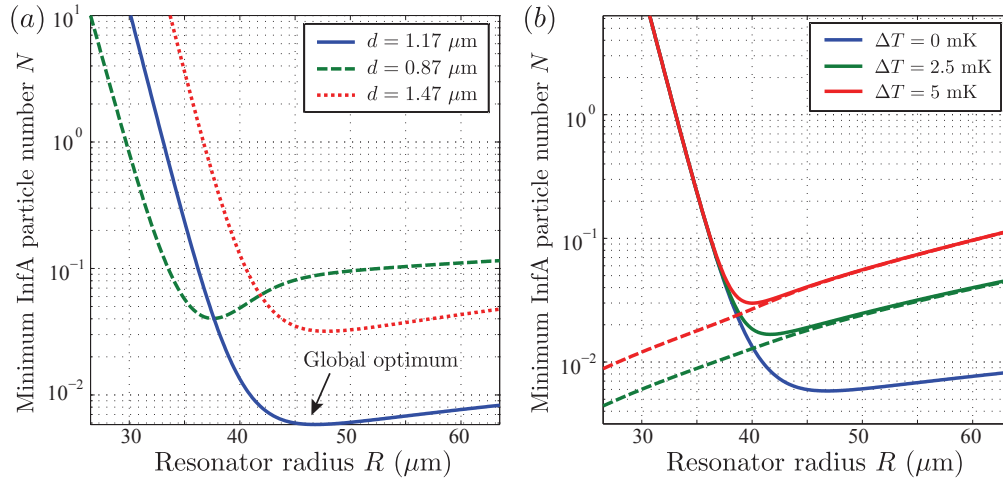


Fig. 3. (a) Minimum detectable number of influenza A (InfA) virions, N as a function of microcavity radius R as set by detector noise for different coupling distances, d . Solid blue curve corresponds to the optimal coupling distance. (b) As (a) for the optimal coupling distance albeit with the addition of thermorefractive noise of varying magnitude as set by the temperature fluctuations ΔT . Solid blue curve corresponds to detector noise only. Dashed curves show detection limits associated with the presence of thermorefractive noise alone. Solid blue lines in (a) and (b) are equivalent.

In light of Eq. (24) it can first be observed that when the coupling distance (and hence coupling loss) is fixed, minimisation of Eq. (24), by means of varying the microcavity size, reduces to the situation discussed in [20] and represents a locally optimal solution. To illustrate this point, Fig. 3(a) shows the calculated N for detection of influenza A (InfA) virions (with refractive index 1.45 and radius 50 nm) using prism coupled ($n_p = 1.77$) fused silica WGM microcavities excited at 780 nm of differing radii and for differing coupling distances. Refractive index data for fused silica and water were taken from [39] and [40] respectively.

Coupling distance can, however, generally be adjusted and provides a further degree of freedom for optimisation in any experimental setup. It can easily be shown analytically that N is minimised when $Q_c/Q_0 = 2$ (or equivalently $A = 0.89$) as depicted in Fig. 4(a). In contradiction to common wisdom, $Q_c/Q_0 = 2$ implies that optimal detection can be achieved when the microresonator is slightly under coupled rather than critically coupled. This result arises since we have shown that optimal detection simultaneously requires a large transmission depth A and a narrow linewidth. Although critical coupling offers the largest transmission depth [41], it also has a slightly larger linewidth than the under coupled regime. Furthermore, with regards to Fig. 4(b) it is evident that the under coupled regime always outperforms the over coupled case by virtue of the higher Q factors for under coupled modes.

For the parameters given above, the optimal sphere radius is found to be $R = 46.8 \mu\text{m}$ with a coupling distance of $1.17 \mu\text{m}$ implying that, at best, $\sim 10^{-2.2}$ InfA virions can be detected at 780 nm, as shown by the solid blue curve in Fig. 3. These calculations were performed assuming only detector noise to be present. Variation of the magnitude of the detector noise, σ_d , merely scales the detection limit N in a linear fashion and does not alter the optimal cavity size. Accordingly, it is also noted that the same optimal sphere radius follows in the case of pink noise. Allowing for the presence of thermorefractive noise (arising from 2.5 mK temperature fluctuations), however, causes the optimal cavity size to drop to $41.6 \mu\text{m}$ whereby $N \approx 10^{-1.7}$.

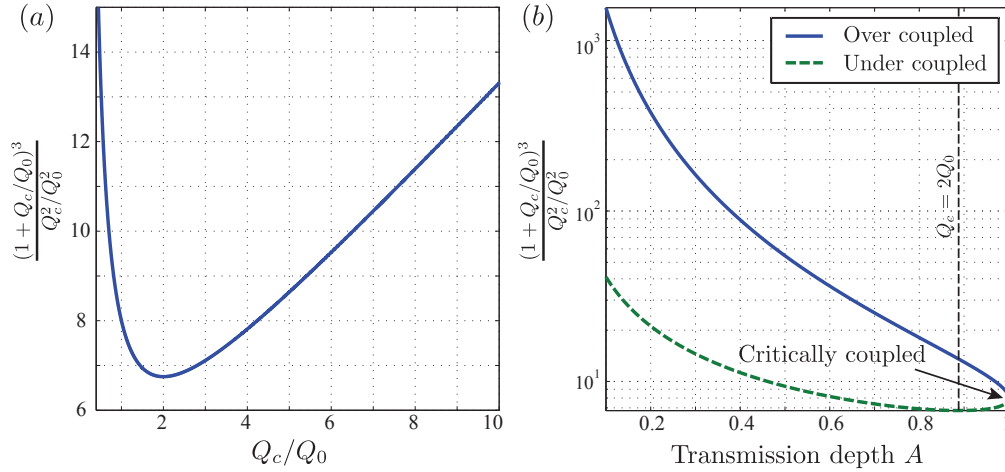


Fig. 4. (a) Variation of $(1 + Q_c/Q_0)^3/(Q_c/Q_0)^2$ factor, describing coupling loss dependence of minimum number of detectable particles, with Q_c/Q_0 . A clear minimum is exhibited at $Q_c = 2Q_0$. (b) Variation of $(1 + Q_c/Q_0)^3/(Q_c/Q_0)^2$ with transmission depth A in the over- and under-coupled regime. Dashed black line corresponds to $A = 0.89$, i.e. $Q_c = 2Q_0$

Evidently, these figures are below the single InfA viron limit given the noise levels chosen.

Whilst Fig. 4 shows an optimal microcavity radius of $46.8 \mu\text{m}$, it is important to mention that this value is strongly dependent on the operating wavelength, principally due to wavelength dependent absorption and dispersion of water. To highlight this point, Table 1 shows the calculated globally optimal microcavity size and coupling distance for a set of common wavelengths ranging from the blue to the infrared end of the optical spectrum. Decreased water absorption in the blue region of the spectrum gives significantly better detection limits than in the red region as would be expected. For example, over two orders of magnitude reduction in N between operating wavelengths of 780 nm and 410 nm can be seen such that when operating at 410 nm detection of a single bovine serum albumin (BSA) is possible. For wavelengths smaller than 410 nm detection limits fall due to increased water absorption. Furthermore, our calculations show that smaller microcavities allow more sensitive measurements in the blue region of the spectrum.

Table 1. Calculated optimal parameters for differing wavelengths. Optimal parameters for detection of BSA monolayer for $\lambda = 1550 \text{ nm}$ and 1300 nm were beyond computational bounds.

| λ (nm) | InfA viron | | | | BSA monolayer | | | |
|-------------------|--------------------|---------------------------------------|---------------------------------------|----------------------------|--------------------|---------------------------------------|---------------------------------------|--|
| | Q_0 | R_{opt} (μm) | d_{opt} (μm) | $\log_{10} N_{\text{opt}}$ | Q_0 | R_{opt} (μm) | d_{opt} (μm) | $\log_{10} \sigma_{s,\text{opt}}$ (m^{-2}) |
| 1550 | 1.30×10^5 | 60.64 | 0.972 | 1.23 | — | > 4000 | — | — |
| 1300 | 1.79×10^5 | 53.07 | 0.866 | 0.92 | — | > 4000 | — | — |
| 780 | 1.51×10^8 | 46.80 | 1.169 | -2.23 | 7.71×10^8 | 202.5 | 1.109 | 10.20 |
| 633 | 1.52×10^9 | 41.18 | 1.127 | -3.41 | 2.00×10^9 | 50.9 | 1.123 | 9.20 |
| 410 | 7.95×10^9 | 26.63 | 0.799 | -4.65 | 8.69×10^9 | 28.2 | 0.799 | 8.32 |

Turning attention to the case of thermorefractive noise, the above analysis can be applied in a similar manner, yielding a measurement acuity of $F = (\sigma_t/\Gamma)(\beta/W)^{1/2}$ and detection limit given by

$$N = \sigma_t \frac{(n_c^2 - n_s^2)}{\text{Re}[\alpha]\omega_0} \frac{R^3}{|Y_{ll}(\pi/2)|^2} \sqrt{\frac{\beta}{W}}. \quad (25)$$

Interestingly, we here see stark differences when compared to the behaviour of detector noise. For example, we note that the detection limit set by thermorefractive noise is independent of coupling and cavity losses and hence scales with an approximate R^3 dependence. Smaller resonators are thus less susceptible to thermorefractive noise for fixed σ_t . Furthermore, smaller cavities imply smaller mode volumes such that the variance of temperature fluctuations, σ_t are also smaller [25]. Illustration of the dependence of N in the presence of pure thermorefractive noise is shown in Fig. 3(b) by the green and red dashed curves for temperature fluctuations of 2.5 and 5 mK respectively. A true R^3 relation is not seen in Fig. 3(b) due to the weak size dependence of the WGM index l . Given the monotonic dependence on R it is immediately apparent, that in contrast to the case of detector noise, no optimal microcavity size exists when thermorefractive noise is dominant.

Realistically, any experimental setup will be subject to both technical and fundamental noise sources. Accordingly the experimental detection limit and optimal microcavity size is set by competing requirements of both noise sources. Formally, noting that the individual noise sources are independent and additive we can employ Stam's inequality and the properties of Fisher information to show $\Delta\omega^2 \geq \Delta\omega_d^2 + \Delta\omega_t^2$. Since we are concerned with the best case scenario we shall hereafter assume equality holds. Intuitively, given the earlier results we would anticipate that the optimal cavity size, in the presence of both detector noise and thermorefractive noise, would be smaller than that for detector noise alone. This expectation is indeed borne out in numerical calculations as shown by the solid curves in Fig. 3(b) for differing magnitude of thermal fluctuations, whereby it can be seen that for large cavities thermorefractive noise is dominant over detector noise, whilst for small cavities the converse holds. Simulation parameters are as above. Given, however, that the optimal cavity size is now set by a balance of competing noise effects it is important to note that the optimal cavity size is dependent on both the sweeping window and sampling rate, since these determine the limit imposed by thermal noise/jitter.

Hitherto we have considered perturbation of a WGM by a single particle, however, studies of monolayers may also be of interest, for example in monitoring self-assembled biological membranes and monolayers [4,42]. In this case it can easily be shown [43,44] that the resonance shift of the WGM for a uniform monolayer of surface density σ_s is

$$\frac{\delta\omega}{\omega_0} = -\frac{\epsilon_s}{(\epsilon_c - \epsilon_s)R} \text{Re}[\alpha]\sigma_s. \quad (26)$$

Letting this shift equal the smallest detectable shift as before, allows the minimum detectable surface density to be determined. We note that the final result is of the same form as Eqs. (24) and (25), albeit for a linear dependence on R (as opposed to R^3) and differing prefactors. The optimal coupling distances is hence once again given by $Q_c/Q_0 = 2$. Figure 5 shows an example calculation of the minimum surface density for a monolayer of BSA. Optimality, for detection of monolayers, is again determined by a balance of competing factors, however for monolayer detection a greater resonator surface area is also desirable because it yields larger absolute resonance shifts. Optimal resonator size is, therefore, significantly larger than for detection of a single particle and, for the same simulations as above, is $R = 202.5 \mu\text{m}$. Optimal cavity size is, however, seen to be much more sensitive to variations in the coupling distance than for single

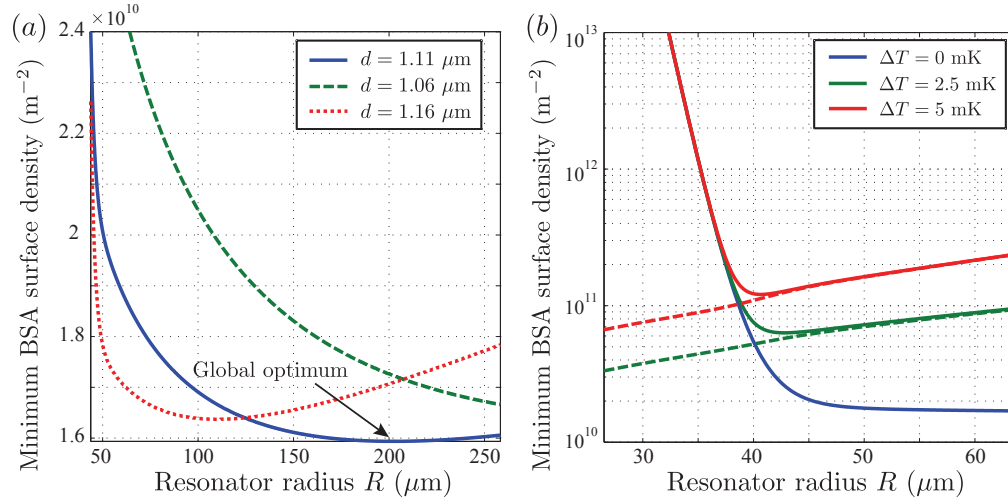


Fig. 5. As Fig. 3, but for detection of a monolayer of BSA molecules.

particle detection (Fig. 5(a)). Addition of thermorefractive noise is seen to reduce the optimal resonator radius as before (Fig. 5(b)).

4.2. Linewidth changes

Upon binding to a microresonator, a particle introduces additional loss mechanisms, namely absorption losses in the particle itself and increased scattering losses. In many scenarios, the associated linewidth change can be detected and provides an alternative and complimentary sensing mechanism to reactive shifts [19]. Whilst Eq. (21) (and subsequent) describe the minimum detectable number of particles when sensing via reactive wavelength shifts, equivalent expressions for monitoring of resonance linewidth can be found. Denoting the linewidth change associated with particle absorption and scattering by $\delta\Gamma_{\text{abs}}$ and $\delta\Gamma_{\text{sca}}$ respectively, we have [45, 46]

$$\frac{\delta\Gamma_{\text{abs}}}{\omega_0} = \frac{\epsilon_s |Y_{ll}(\pi/2)|^2}{(\epsilon_c - \epsilon_s) R^3} \text{Im}[\alpha], \quad (27)$$

$$\frac{\delta\Gamma_{\text{sca}}}{\omega_0} = \frac{\omega_0^3 n_s^5 |Y_{ll}(\pi/2)|^2}{3\pi c^3 (\epsilon_c - \epsilon_s) R^3} |\alpha|^2, \quad (28)$$

where c is the speed of light. Emphasis must be made, however, that these expressions are not valid in the case of mode splitting, which has also been proposed as a further sensing mechanism [14, 47]. For dielectric particles at wavelengths far from molecular resonances, the latter is dominant and yields a minimum detectable number of particles of

$$N = \frac{\Delta\Gamma}{\delta\Gamma_{\text{sca}}} = \frac{6\pi c^3 (n_c^2 - n_s^2)}{|\alpha|^2 n_s^5 \omega_0^3} \frac{R^3}{|Y_{ll}(\pi/2)|^2} \frac{F_0}{Q_0} \frac{(1 + Q_c/Q_0)^3}{4Q_c^2/Q_0^2} \quad (29)$$

for detector noise, where F_0 is as defined above and

$$N = \sigma_l \frac{6\pi c^3 (n_c^2 - n_s^2)}{|\alpha|^2 n_s^5 \omega_0^4} \frac{R^3}{|Y_{ll}(\pi/2)|^2} \sqrt{\frac{3\beta}{W^3}} \quad (30)$$

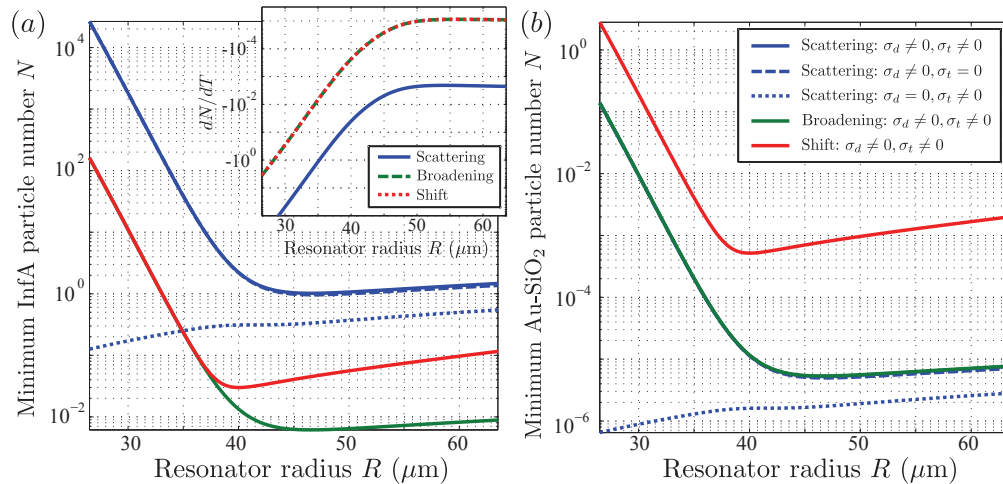


Fig. 6. (a) Comparison of minimum detectable number of influenza virions, N as a function of microcavity radius R when monitoring linewidth changes (blue and green) or resonance frequency shift (red). Blue curves depict detection limits when broadening is dominated by particle induced scattering losses for different noise sources. Green curves show detection limits for broadening considering all particle induced broadening mechanisms. (b) As (a) albeit for a 60 nm radius gold-silica nanoshells with resonance tuned to match the probing WGM frequency. (inset) Dependence of dN/dT with respect to microcavity radius.

for thermorefractive noise. Blue curves in Fig. 6(a) depict the limits imposed on detection of single InfA virions using linewidth broadening when scattering losses are the dominant broadening process (dashed curve corresponds to detector noise only, dotted curve corresponds to thermorefractive noise only and solid curve corresponds to the presence of both noise sources). Of particular note is that thermorefractive noise plays a less significant role than detector noise, such that an optimal cavity radius can again be identified.

Absorption in the particle can also significantly affect the linewidth broadening of a WGM, especially if the analyte comprises metallic nanoparticles or fluorescent emitters (or if these are used as labels) [12, 48, 49]. In this case the linewidth change is given by $\delta\Gamma = \delta\Gamma_{\text{sca}} + \delta\Gamma_{\text{abs}} + \delta\Gamma_{\text{cc}}$. The additional $\delta\Gamma_{\text{cc}}$ term has also been included since the presence of a scattering particle on a microresonator couples light into a (initially degenerate) counter-propagating WGM [50]. When coupling is not strong enough to induced mode splitting, the unresolved splitting of the two counter-propagating WGMs yields an additional broadening of magnitude $\delta\Gamma_{\text{cc}} = 2|\delta\omega|$ [14, 51]. Since these additional induced loss mechanisms cause greater line broadening, the particle induced changes in lineshape are larger and thus the associated detection limit is better than when only scattering losses are present. Figure 6(a) highlights this point by considering the detection limits, for influenza virions, associated with scattering losses only (blue curves), as compared to inclusion of all broadening mechanisms, i.e. scattering, absorption and coupling to counter-propagating modes (solid green curve). Additionally, and for comparison purposes, the detection limit for sensing using reactive shifts is also shown in Fig. 6(a) (red curve). Similar detection sensitivity is exhibited by both detection modalities for cavity sizes $\lesssim 39 \mu\text{m}$, however, as the microresonator size increases thermorefractive noise begins to dominant the reactive shift detection limit, whilst sensing via line broadening is only weakly affected (as discussed above). Ultimately biosensing via mode broadening is predicted to have the better detection limit, with appropriate optimisation of cavity size and coupling dis-

tance. Similar results were found in [19]. When particle absorption is large, e.g. for resonant plasmonic nanoparticles, sensing via monitoring linewidth changes is superior for all cavity sizes. To illustrate this point Fig. 6(b) shows the limits for detection of 60 nm radius gold-silica nanoshells with plasmon resonance tuned to 780 nm i.e. to match the WGM frequency, whereby over an order of magnitude is gained in detection sensitivity compared to the shift based modality.

5. Thermal stability

Bulk temperature drifts are routinely present in biosensing experiments as evidenced by long term trends in the WGM resonance frequency. However, given the thermal dependencies of the refractive indices of both the microcavity and surrounding host medium, any temperature drifts will also cause a change in the detection sensitivity as described by Eqs. (24), (25), (29) and (30). Robustness to such thermal drifts is naturally desirable in an experimental environment, such that the question as to the least temperature sensitive WGM sensor can be posed. Assuming temperature drifts to be relatively small, we can consider the Taylor expansion $N(T) = N(T_0) + (T - T_0)dN/dT + \dots$, such that we can use the temperature gradient of the minimum detectable number of particles dN/dT to quantitatively assess thermal stability of our previously derived detection limits. Restricting to detector noise only, the temperature derivatives of Eqs. (24) and (25) can be determined (for simplicity we consider only the temperature variation of the real part of the refractive indices of the cavity and surrounding water, where we take $dn_s/dT = -8.33 \times 10^{-5}$ [52]). The results of such a calculation, assuming the same simulation parameters as previously, are shown in the inset of Fig. 6(a) for both shift and broadening sensing scenarios. Very similar temperature sensitivity is seen in both cases, however, when scattering losses dominate other broadening mechanisms the temperature sensitivity is greater, due to the n_s^3 dependence of the scattering losses. Notably, the temperature gradient is negative, such that temperature increases improve sensitivity and vice-versa, primarily because a temperature increase causes the refractive index contrast between the microcavity and host medium to increase. Furthermore an optimal microresonator size can be identified, that is to say a cavity size exhibiting minimal variation in detection sensitivity with temperature. In all calculations performed the most temperature stable cavity was found to have a larger radius than the optimal size associated with minimising N . Use of larger resonators is thus seen to be experimentally beneficial, however the choice of cavity size, will depend on the relative importance assigned to detection sensitivity and temperature stability. Naturally, other considerations, such as space restrictions for on-chip integration and fabrication capabilities may also play a determining role.

6. Additional losses

Commonly, in any experimental realisation of a WGM biosensing experiment, the observed Q factor is lower than theoretical expectations when considering only the intrinsic, absorption and coupling losses. Such additional losses, can for example arise from surface roughness, scattering defects in the resonator structure (e.g. air bubbles) and non-sphericity of the resonator. Furthermore, in plasmon enhanced sensing the presence of the nanoantenna gives rise to additional scattering and heating losses (see Section 4.2). The question then arises as to how additional losses affect the preceding results. To address this problem it is necessary to return to Eq. (21), which we write in the form $N = C(R)F_0/AQ$, where now $Q^{-1} = Q_0^{-1} + Q_c^{-1} + Q_m^{-1}$ and Q_m denotes the additional miscellaneous losses. As before we can consider the optimisation of the coupling distance and the resonator size independently. Fuller mathematical details are given in Appendix C, however, we find that the new optimal coupling distance satisfies the

relation

$$\frac{Q_c}{Q_0} = \frac{1}{2} \left[1 + \sqrt{\frac{1+9Q_m}{1+Q_m}} \right] \approx 2 - \frac{2}{3Q_m}, \quad (31)$$

where the latter approximation holds when $Q_m^{-1} \ll 1$. Subsequently optimisation of the resonator size yields a shift in the optimal resonator size of

$$\delta R \approx \frac{2C(R_{\text{opt}})}{Q_0 Q_m} \frac{\partial Q_m}{\partial R} \left[(3Q_m + 2) \frac{\partial^2 [C(R)/Q_0]}{\partial R^2} \Big|_{R=R_{\text{opt}}} \right]^{-1}. \quad (32)$$

With the possible exception of $\partial Q_m/\partial R$, all quantities in Eq. (32) are positive. Consequently, $\partial Q_m/\partial R$ dictates whether the optimal resonator size increases or decreases. For example, for mechanisms whereby losses increase with the resonator size, such as surface roughness and defect scattering, $\partial Q_m/\partial R$ is negative, such the optimal resonator size decreases. In contrast, however, given that larger microcavities have a larger proportion of the mode lying within the resonator, scattering losses from nanoantenna decrease with larger resonator size. Consequently $\partial Q_m/\partial R$ is positive, hence motivating the use of larger resonators. Equivalent results follow when considering line broadening as a sensing mechanism.

7. Conclusions

In this article we have adopted an information theoretical framework within which the detection limits of a spherical microresonator based biosensor have been formally derived. A suitable noise model was required in the derivations, such that, motivated by experimental and previous theoretical findings, we considered two specific cases: technical (detector) and thermorefractive noise. Firstly, technical noise in the form of additive Gaussian noise, as may arise from stray light, was considered, whereby it was found that both the minimum resolvable frequency shift and linewidth change scaled linearly with linewidth and with the square root of the sampling interval. Contrasting results were, however, found when thermorefractive noise/laser jitter was considered, whereby weak dependence on the resonance linewidth was found. Dependence on the sampling interval remained however, and an inverse relationship with the sweeping window was also found, i.e. a larger laser sweep (for fixed sampling) allows greater measurement accuracy.

To facilitate utility within a biosensing context, we further applied the derived detection limits to the question of the minimum number of detectable bioparticles (and surface density of a monolayer). Numerical calculations were also presented based on detection of InfA virions and BSA monolayers. In the presence of detector noise a clear optimal microcavity size can be identified arising from balancing the requirements of narrow linewidth, small mode volume and large surface intensity. Attention was limited to first radial order WGMs, however, it is important to mention that the optimal cavity size increases as the radial number increases. Coupling to the correct mode is therefore important in realising potential gains offered by optimising microcavity size. Sensor surface area was also found to play an important role for detection of monolayers, such that optimal cavity sizes were found to be significantly larger than for single particle detection. Interestingly, our results show that from an experimental point of view it can be better to air on the side of caution when fabricating microspheres so as to produce larger than desired spheres. This paradigm can be understood by observing that loss of detection sensitivity is more severe for smaller than optimal cavity sizes than the reverse case (see e.g. Fig. 3). This point is further seen when considering the stability of detection limits to long term temperature drifts. No optimal resonator size exists in the case of thermorefractive noise

alone, however when both noise sources are present, the optimum size is reduced, dependent on the relative magnitude of each noise source. In addition to optimising the microresonator radius, use of Fisher information underlined the role of coupling losses in setting detection limits, hence allowing a further degree of freedom in system design. Specifically, and in opposition to common opinion, a critically coupled cavity was found to be less sensitive than a moderately under coupled one.

The analysis and discussion given, was found to hold true when either induced changes in resonance frequency or linewidth were monitored. Relative performance of the sensing modalities however is dependent on the properties of the particles of interest. Non-absorbing particles imply comparable performance between both modalities for smaller resonators, albeit broadening based sensing surpasses the more common reactive shift based sensing for larger microcavities and when absorption in the particle is strong. Careful assessment of the specific detection task at hand is therefore necessary in system design.

A. Appendix A - Justification for neglecting temperature dependent line broadening

To study the dependence of the resonance frequency and linewidth of a WGM in a microsphere, we must recall the resonance condition for Mie resonances i.e.

$$\frac{[n_s z h_l(n_s z)]'}{h_l(n_s z)} = N \frac{[n_c z j_l(n_c z)]'}{j_l(n_c z)}, \quad (33)$$

where $N = 1$ or $(n_s/n_c)^2$ for TE or TM modes respectively, $j_l(x)$ and $h_l(x)$ are the spherical Bessel and Hankel functions of the first kind, $z = ka$, k is the (complex) vacuum wavenumber, a is the resonator radius, prime denotes differentiation with respect to the argument of the respective Hankel or Bessel function and n_s (n_c) is the refractive index of the surrounding medium (resonator). From Eq. (33) it has previously been shown that the spectral position and linewidth (neglecting absorption) of high Q WGMs can be expressed by asymptotic expressions [53], which when written in our notation take the form

$$z_0 \approx \frac{l + 1/2}{n_c} + \dots \quad (34)$$

$$\Gamma \approx \frac{2c}{a(n_c^2 - n_s^2)} \frac{1}{n_s z_0^2 y_l^2(n_s z_0)} \quad (35)$$

where $y_l(x)$ are the spherical Neumann functions. We note we make no restriction to resonators in air as done in [53]. Considering then TE modes for definiteness we can show by differentiating Eqs. (34) and (35) and using standard properties of the spherical Neumann functions [34], that the ratio

$$\rho = \frac{d\Gamma/dT}{d\omega_0/dT} = \frac{d\Gamma/dn_c}{d\omega_0/dn_c} = \frac{2}{Q} \left(\frac{n_s^2}{n_c^2 - n_s^2} - n_s z_0 \frac{ly_{l-1}(n_s z_0) - (l+1)y_{l+1}(n_s z_0)}{(2l+1)y_l(n_s z_0)} \right). \quad (36)$$

Terms within the parentheses are of order $z_0 \sim l \sim 10^2$, such that the $1/Q$ factor dominates. Eq. (36) therefore demonstrates that the variation in the linewidth from temperature fluctuations is many orders of magnitude smaller than the variation in the resonance frequency since WGMs possess high Q factors. Whilst algebraically more involved, the derivation for TM modes similar conclusions.

B. Appendix B - Derivation of $J_{\Gamma,\Gamma}$ in the presence of thermorefractive noise

Our derivation starts by noting

$$J_{\Gamma,\Gamma} = \sum_{j=1}^{N_\Omega} \int_0^\infty \left[1 + \frac{\Lambda_j^2}{\sigma_t^2} - \frac{\Lambda_j^2 \Delta_j}{\sigma_t^4} \operatorname{sech}^2 \left(\frac{\Lambda_j \Delta_j}{\sigma_t^2} \right) \right] \frac{1}{\Gamma^2} p_{I_{d,j}} dI_{d,j}. \quad (37)$$

Evaluating the summation for the first term exactly and approximating the summation as an integral in the second and third terms as before yields

$$J_{\Gamma,\Gamma} \approx \frac{N_\Omega}{\Gamma^2} + \frac{\sqrt{2/\pi}}{\Gamma^2 \Delta \Omega \sigma_t} \left\{ \int_0^\infty \exp \left(-\frac{\Lambda^2}{2\sigma_t^2} \right) \int_{-\Omega/2}^{\Omega/2} \left[\frac{\Lambda^2}{\sigma_t^2} \cosh \left(\frac{\Lambda \Delta}{\sigma_t^2} \right) \right] \exp \left(-\frac{\Delta^2}{2\sigma_t^2} \right) d\Delta d\Lambda \right. \\ \left. - \int_0^\infty \exp \left(-\frac{\Lambda^2}{2\sigma_t^2} \right) \int_{-\Omega/2}^{\Omega/2} \left[\frac{\Lambda^2 \Delta^2}{\sigma_t^4} \operatorname{sech} \left(\frac{\Lambda \Delta}{\sigma_t^2} \right) \right] \exp \left(-\frac{\Delta^2}{2\sigma_t^2} \right) d\Delta d\Lambda \right\}. \quad (38)$$

The third term can be treated in an analogous manner to the integral in Eq. (13) by again making the approximation $\operatorname{sech} x \approx \exp[-x^2/2]$ to yield

$$J_{\Gamma,\Gamma} \approx \frac{N_\Omega}{\Gamma^2} + \frac{\sqrt{2/\pi}}{\Gamma^2 \Delta \Omega \sigma_t} \int_0^\infty \exp \left(-\frac{\Lambda^2}{2\sigma_t^2} \right) \int_{-X_\Omega}^{X_\Omega} \cosh x \exp \left(-\frac{x^2 \sigma_t^2}{2 \Lambda^2} \right) dx d\Lambda - \frac{0.563 \sigma_t}{\Gamma^2 \Delta \Omega} \quad (39)$$

where the change of variables $x = \Lambda \Delta / \sigma_t^2$ has been made. Upon performing the integration over x the second term becomes

$$\frac{1}{\Gamma^2 \Delta \Omega \sigma_t^2} \int_0^\infty \Lambda^2 \left[\operatorname{erf} \left(\frac{Z \sigma_t + \Lambda}{\sqrt{2} \sigma_t} \right) + \operatorname{erf} \left(\frac{Z \sigma_t - \Lambda}{\sqrt{2} \sigma_t} \right) \right] d\Lambda \quad (40)$$

where $2Z = \Omega / \sigma_t$ and erf denotes the error function. Noting that the error function is an odd function and that $\operatorname{erf}(2) = 0.995 \approx 1$ the kernel can be taken as zero for $\Lambda > (Z + 2\sqrt{2})\sigma_t$. Further neglecting $\exp(-4)$ terms after integration of the resulting finite definite integral (40) yields

$$J_{\Gamma,\Gamma} \approx \frac{N_\Omega}{\Gamma^2} + \frac{2\sigma_t}{3\Gamma^2 \Delta \Omega} Z(3 + Z^2) - \frac{0.563 \sigma_t}{\Gamma^2 \Delta \Omega} = \frac{\Omega}{\Gamma^3} \frac{6Z + Z^3 - 0.845}{3\beta Z}. \quad (41)$$

Finally noting that $Z \gg 0.845$ for realistic scenarios Eq. (16) quickly follows.

C. Appendix C - Derivation of Eqs. (31) and (32)

Consider Eq. (21) which we write in the form $N = C(R)F_0/AQ$ where

$$C(R) = \frac{(n_c^2 - n_s^2)}{\operatorname{Re}[\alpha]} \frac{R^3}{|Y_{II}(\pi/2)|^2}. \quad (42)$$

Substituting in $A = 4Q_0 Q_c / (Q_0 + Q_c)^2$ and $Q^{-1} = Q_0^{-1} + Q_c^{-1} + Q_m^{-1}$ yields

$$N = \frac{C(R)F_0}{Q_0} \frac{(1 + Q_c/Q_0)^2}{4Q_c/Q_0} \left(\frac{1 + Q_c/Q_0}{Q_c/Q_0} + \frac{1}{Q_m} \right). \quad (43)$$

Letting $f_1(R) = C(R)F_0/Q_0$ and $f_2 = N/f_1$, we can write

$$\frac{dN}{dR} = \frac{\partial f_1}{\partial R} f_2 + f_1 \frac{\partial f_2}{\partial Q_m} \frac{\partial Q_m}{\partial R} + f_1 \frac{\partial f_2}{\partial x} \frac{\partial x}{\partial R}, \quad (44)$$

where $x = Q_c/Q_0$. We wish to find the conditions under which $dN/dR = 0$. Variation of the coupling losses Q_c by means of adjusting the coupling distance allows us to first zero the third term of Eq. (44) by setting $\partial f_2/\partial x = 0$. Noting the requirement that $x > 0$ it quickly follows that $\partial f_2/\partial x = 0$ when Eq. (31) holds. In the limit that $1/Q_m \rightarrow 0$ the result of Section 4 (i.e. $Q_c/Q_0 = 2$) is restored. Upon optimisation of the coupling distance we thus determine the optimal microcavity radius by solution of

$$\frac{\partial f_1}{\partial R} \left(\frac{27}{16} + \frac{9}{8Q_m} \right) - f_1 \frac{\partial Q_m}{\partial R} \frac{9}{8Q_m^2} = 0, \quad (45)$$

which follows by substitution of Eq. (31) into Eq. (44), expanding in terms of Q_m^{-1} and equating to zero. Further performing a Taylor expansion of $f_1(R)$ about the optimal radius size for $Q_m^{-1} = 0$ (i.e. R_{opt}) and noting $\partial f_1/\partial R|_{R=R_{\text{opt}}} = 0$ yields

$$\left. \frac{\partial^2 f_1}{\partial R^2} \right|_{R=R_{\text{opt}}} \delta R \left(\frac{27}{16} + \frac{9}{8Q_m} \right) - f_1(R_{\text{opt}}) \frac{\partial Q_m}{\partial R} = 0, \quad (46)$$

where δR is the change in the optimal microcavity radius from introduction of Q_m . Rearrangement of Eq. (46) yields Eq. (32).

Acknowledgments

We gratefully acknowledge financial support for this work from the Max Planck Society (FV), the Alexander von Humboldt Foundation (MRF), the National Undergraduate Innovational Experimentation Program and the National Fund for Fostering Talents of Basic Science (WLJ - Grant No. J1030310 and No. J1103205).